Available online at www.sciencedirect.com
SCIENCE DIRECT®

Journal of the European Ceramic Society 23 (2003) 1675–1685
www.elsevier.com/locate/jeurceramsoc

A phenomenological constitutive model for the sintering of alumina powder

HongGee Kim[1], Olivier Gillia[2], Didier Bouvard*

Laboratoire Génie Physique et Mécanique des Matériaux, Institut National Polytechnique de Grenoble/CNRS, Saint Martin d'Hères, France

Received 8 February 2002; received in revised form 21 October 2002; accepted 28 October 2002

Abstract

This paper develops a phenomenological model for the densification and viscous behavior of alumina powder during sintering. The free sintering strain rate part and the viscoplastic strain rate part of the constitutive model were determined from experimental data by using the experimental method proposed for WC–Co mixture by Bouvard and co-workers. From densification data under free sintering by using reference and stairway heating cycles with samples of three different green densities, a simple densification equation was identified. This equation expresses the densification rate as a function of temperature, relative density, and green density. The predictive capability of the identified densification equation was discussed by investigating the densification of alumina powder during various sintering cycles and with different green densities. For the viscoplastic strain rate part of the constitutive model, the axial viscosity and the viscous Poisson's ratio of an alumina powder compact were determined by using an intermittent loading method.

Keywords: Al_2O_3; Constitutive model; Modelling; Sintering

1. Introduction

To produce high quality components, ceramic products must be manufactured to near-net-shape with controlled microstructure.[1] Thus, successful near-net-shape forming of powder components requires the theoretical study and the development of proper constitutive models that can predict densification behavior under sintering. Especially, when the density distribution in a powder compact is heterogeneous, the densification is not uniform and the shape of the component does not change in a self-similar fashion during sintering. So far, extensive efforts[2–6] have been carried out for the prediction of densification kinetics for powder compacts. The shape change of powder compacts has been investigated recently with the help of numerical methods.[3,7–9] For those purposes, an analytical description of the densification rate of the powder system as a function of relevant material and process parameters is required.

Many authors[2–4,10–13] attempted to obtain such a description by the modeling of physical mechanisms for sintering. Most of them derived the densification kinetics of a powder aggregate from the sintering of two contacting spheres by viscous flow or diffusion phenomena. Analytical equations have been proposed to investigate the two-sphere problem and derive the macroscopic behavior.[2,10,11] Later on, numerical methods gave a more realistic description of interparticle neck geometry, the coupling of several diffusion mechanisms, and the processing of a large number of randomly packed particles.[12,13] After more or less empirical adjustments for the physical parameters, these models succeeded in describing experimental results for a given material. However, it would likely require parameter adjustments again to apply the models to other materials. Hence, though the microstructural approach is certainly useful in understanding the physics of sintering, to identify the dominant densification mechanism, and to predict the microstructural changes, it is of little interest for an effective control of the densification process.[14]

* Corresponding author.
E-mail address: didier.bouvard@inpg.fr (D. Bouvard).
[1] Present address: Metal Forming CAD/CAE Lab., Pohang University of Science and Technology, Pohang, South Korea.
[2] Present address: CEA, Grenoble, France.

0955-2219/02/$ - see front matter
PII: S0955-2219(02)00411-9

An alternative approach is phenomenological modeling,[4,15,16] which consists of fitting analytical expressions directly from the results of sintering experiments. Thus, it provides a constitutive equation describing as precisely as possible the real behavior of the material. Most often these expressions are assumed to be formally close to the equations predicted by microstructural models, but the parameters are adjusted from the experimental data without regarding their physical meaning.

The present work used a phenomenological approach to describe the densification kinetics of alumina powder during sintering. Experimental data were obtained by using the experimental method proposed for WC–Co mixture by Gillia and co-workers.[15,16] From these data a simple densification equation was identified. This equation expresses the densification rate as a function of temperature, relative density and green density, which seem to be the minimal set of relevant variables. The predictive capability of the identified densification equation was discussed by investigating the densification of the material during various sintering cycles and for different green densities. To determine the parameters for the viscoplastic strain rate part of the constitutive model, the axial viscosity and the viscous Poisson's ratio of an alumina powder compact were obtained by using an intermittent loading method under uniaxial compression at various temperatures with samples having three different green densities.

2. Constitutive model

During the last decade, many attempts were made to simulate the conventional sintering of industrial parts.[17–19] A particular interest has been shown for shape changes during sintering and for the sintering of materials with poor compressibility such as hard materials or ceramics. These materials suffer large shrinkage and the final shape of sintered parts is often non-scale invariant due to non-homogeneous density field, gravity effects or anisotropy. Since stresses may arise in the part, it is necessary to know the behavior of the material under these stresses. To describe this behavior, a general model based on a Newtonian constitutive equation has been extensively used.[17–19] This choice suggests that the stress level is low enough so that linearity between stress and strain rate tensors can be assumed. The hydrostatic and the deviatoric effects are separated through the definition of two viscosities, K and G, respectively the bulk and the deviatoric viscosity. The constitutive equation is written:

$$\tilde{\dot{\varepsilon}}^{tot} = \frac{-P+\sigma_s}{3K}\tilde{I} + \frac{1}{2G}\tilde{\sigma'} + \tilde{\dot{\varepsilon}}^{rev} \tag{1}$$

where $\tilde{\dot{\varepsilon}}^{tot}$, $\tilde{\dot{\varepsilon}}^{rev}$, $\tilde{I}$, and $\tilde{\sigma'}$ are, respectively, the total strain rate tensor, the reversible strain rate tensor (including elasticity and thermal expansion), the identity tensor, and the deviatoric stress tensor. Also P is the hydrostatic pressure and σ_s is the sintering stress, i.e. the thermodynamic force associated with densification.[19] The sintering stress can also be defined as the opposite of the isotropic pressure that would stop densification. Shrinkage during free sintering is introduced through the sintering stress.

It appears that the non-reversible strain rate can be split into two parts, the free sintering strain rate, $\tilde{\dot{\varepsilon}}^{s}$ and the viscoplastic strain rate, $\tilde{\dot{\varepsilon}}^{vp}$. We can define the free sintering strain rate and the viscoplastic strain rate as follows:

$$\tilde{\dot{\varepsilon}}^{\mathrm{s}} = \frac{\sigma_{\mathrm{s}}}{3K}\tilde{I} \tag{2}$$

$$\tilde{\dot{\varepsilon}}^{\mathrm{vp}} = -\frac{P}{3K}\tilde{I} + \frac{1}{2G}\tilde{\sigma'} \tag{3}$$

Finally, we can express the total strain rate as follows:

$$\tilde{\dot{\varepsilon}}^{\mathrm{tot}} = \tilde{\dot{\varepsilon}}^{\mathrm{s}} + \tilde{\dot{\varepsilon}}^{\mathrm{vp}} + \tilde{\dot{\varepsilon}}^{\mathrm{rev}} \tag{4}$$

We should recall that this relation is valid only under the assumption of a Newtonian law.

To define the viscoplastic part of the constitutive model, the parameters K and G have to be determined. Generally K and G are dependent on internal variables since the properties of the material strongly evolve during sintering. The variables most often used are temperature and density. Sometimes the grain size is considered as a complementary variable and numerous other choices are possible. However, in experimental investigation, it is more convenient to determine the equivalent pair (the axial viscosity, η_z and the viscous Poisson ratio, ν^{vp}) that can be defined as

$$\eta_{\mathrm{z}} = \frac{\dot{\varepsilon}_z^{\mathrm{vp}}}{\sigma_{\mathrm{z}}} \tag{5}$$

$$\nu^{\mathrm{vp}} = -\frac{\dot{\varepsilon}_{\mathrm{r}}^{\mathrm{vp}}}{\dot{\varepsilon}_z^{\mathrm{vp}}} \tag{6}$$

where the index z indicates the direction of loading and r indicates a perpendicular direction. Thus, K and G can be calculated from:

$$K = \frac{\eta_{\mathrm{z}}}{3(1-2\nu^{\mathrm{vp}})} \tag{7}$$

$$G = \frac{\eta_z}{2(1+\nu^{\mathrm{vp}})} \tag{8}$$

3. Experiments

3.1. Sample preparation

The powder used in this paper has been obtained by granulation of micronic alumina particles. It contains

5% in weight of sintering additive composed of silica and magnesium oxide, as well as organic components required for the granulation, which are eliminated before sintering. The loose density ranges from 1.08 to 1.24 g/cm^3 depending on the filtering procedure. Cylindrical compacts of 6 mm diameter and 9 mm height were prepared by double action die pressing with several compacting stresses between 40 and 700 MPa. The relative density, D, is defined as the mass density of the sample divided by the theoretical density of pure alumina at room temperature, 3.98 g/cm^3. We thus neglect the presence of sintering additives for the calculation of the relative density. The error resulting from this simplification is estimated to be less than 2%. The samples had green relative densities, D_o, between 0.53 and 0.67. Most tests have been performed with compacts with a green relative density, $D_{o,ref} = 0.59$, which will be referred to as the 'reference green density'. Since the powder compact contains some organic components as binders that can pollute the experimental apparatus, the organic components were removed at 350 °C under air for 30 min.

For bending experiments, powder compacts of 3.06 mm in height, 3.33 mm in width, and 15.31 mm in length were prepared in a rectangular die by double action pressing at 200 MPa. Since the compacts were fragile enough to be broken during the loading, they were pre-sintered at 1050 °C for 1 h to have moderate strength without densification. The samples had the average green relative density, $D_o = 0.61$.

3.2. Free sintering

The compacts were sintered in air in a dilatometer (TMA92, SETARAM, France), which allows application of an axial loading during sintering. This apparatus measures the length variation of a sample in a ±2000 μm range with 4 μm accuracy. However the interaction between the alumina push rod and the sample decreases the accuracy to about 25 μm.[15] Throughout the test, a load of 5 g is applied upon the rod to ensure its contact with the sample. It has been verified that this small load has no influence on the deformation of the sample. The heating cycles were as shown in Fig. 1. For the reference cycle, a uniform heating rate (6 °C/min) was applied. A cycle with five isothermal sequences between 1300 and 1575 °C has been also adapted following the reference cycle according to the method described in Gillia and Bouvard.[15] It will be called the 'stairway cycle' in the following. After a holding time at 1575 °C, the sample was cooled naturally by turning off the heating power.

Densification of Al_2O_3–SiO_2–MgO systems mainly operates by liquid phase sintering. The liquid phase that appears during heating wets alumina interparticle contacts and then classical liquid phase sintering mechanisms are activated, particle rearrangement under capillary forces and dissolution-reprecipitation of Al_2O_3 in the liquid phase.[20] Fig. 2 shows a SEM picture of a sample with $D_o = 0.67$ after the reference sintering cycle. It can be observed that most alumina grains have grown up to a few micron sizes and show an elongated shape. They are separated either by residual pores (black) or by a vitreous phase (darker grey) formed during cooling.

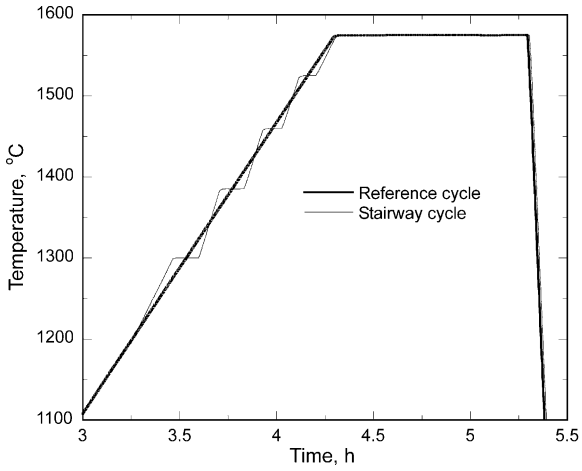

Fig. 1. Heating cycles of the reference and the stairway tests.

3.3. Viscosities

Axial viscosity was investigated in air using the SETARAM dilatometer. The applied stress has to be typically of the order of magnitude of the sintering stress. The axial stress created by a load of 85 g was about 0.03 MPa, which was enough to modify the densification kinetics. The axial viscosity of an alumina powder compact during sintering was investigated with the help of the intermittent loading method proposed by Cai et al.[21] and Gillia et al.[16] A continuous load may induce a severe mechanical history that undoubtedly affects the behavior of the material. Thus, rather than a continuous load, an intermittent load was applied to the sample. For example, Fig. 3 shows the heating and loading cycle for intermittent loading during a long isothermal period at 1400 °C.

The viscosity was also investigated from bending tests in air using the SETARAM dilatometer. A three-point bending jig was made of alumina and placed in the dilatometer. The distance (span length) between two lower supports is 12 mm. A constant heating rate of 6 °C/min was first applied up to different temperatures; then, during temperature holding, a constant load of 15 g was continuously applied on the center of the sample. Since the sample may have some deflection due to its weight, experiments with a constant load of 2 g were also carried out for reference data. Therefore, the deflection data due to the stress caused by the applied load of 13 g can be obtained by subtracting the deflection data with 2 g from that with 15 g. Then, the viscosity was calculated

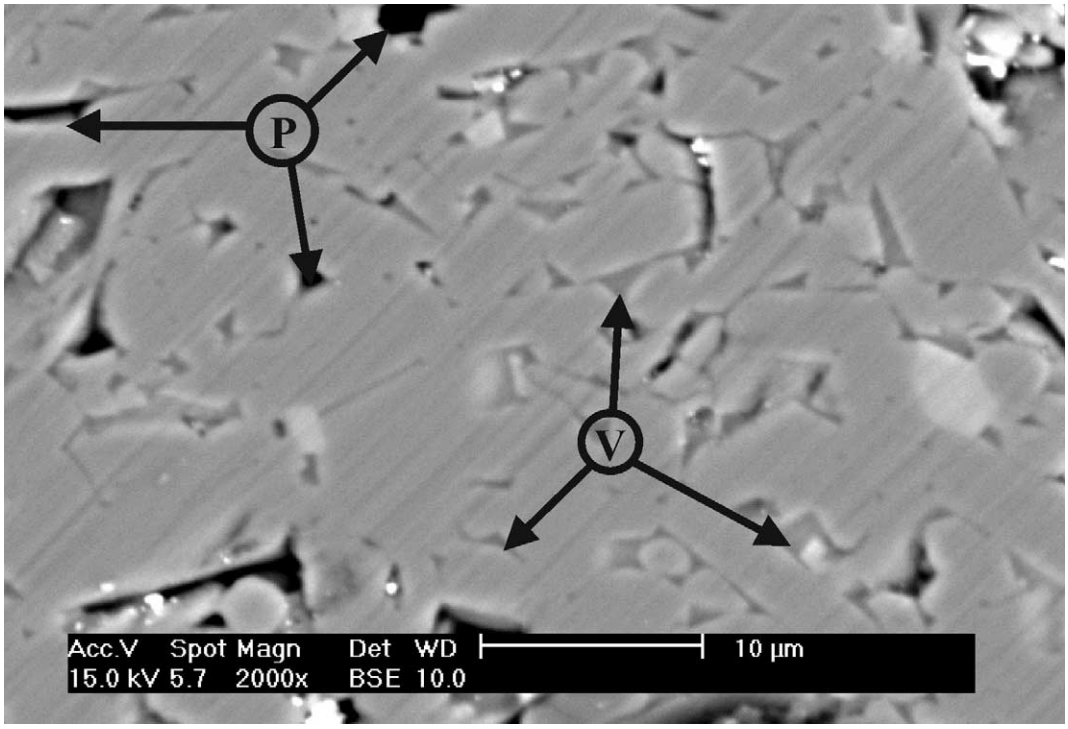

Fig. 2. SEM image of an alumina sample after the reference heating cycle. Some residual pores and vitreous phase regions are marked with 'P' and 'V', respectively.

from the measured deflection data of the sample by using the analogy between elastic and viscous theories that will be explained later in this paper.

The viscous Poisson's ratio was investigated under vacuum using a furnace mounted on a mechanical testing press. Two quartz windows were set in opposite sides of the wall of the furnace in order to observe the deformation of the sample at the experimental temperature with a 1000×1000 CCD video camera. After holding for 5 min at the experimental temperature, the upper punch was set in contact with the sample and was driven down at a constant speed of 0.001 mm/s. At that time, the force increases and the diameter of the sample also increases significantly. The downward movement of the upper punch was then stopped after which the force and the diameter of the sample decrease. This scheme (moving down and pause of upper punch) was repeated to the end of the experiment with the force increasing each time. The detailed method can be found in the literature.[16] From the camera image, the average diameter and the height of the sample during the experiment were calculated. Unfortunately the maximum temperature of the furnace was 1340 °C, thus, the experiment for viscous Poisson's ratio was carried out at this temperature only.

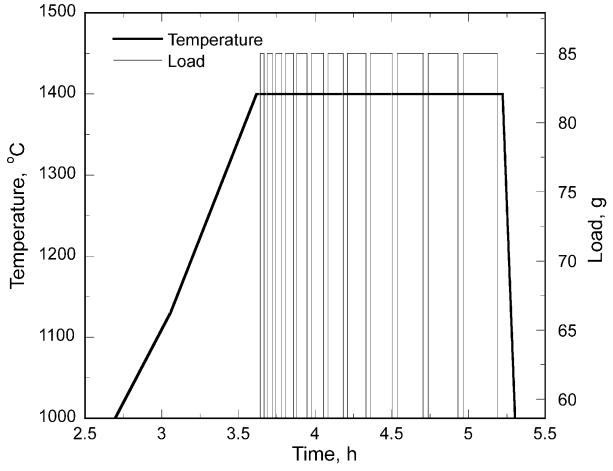

Fig. 3. Heating and loading cycles for intermittent loading experiment.

4. Results and analysis

4.1. Free sintering

Fig. 4 shows the densification behavior of an alumina powder compact with reference green density under the reference and stairway cycles. It can be observed that all isothermal sequences are approximately centered with respect to the reference cycle. It can be also observed that the densification starts around 1100 °C.

Fig. 5 shows the experimental data for the densification rate of an alumina powder compact with reference green density under the reference and stairway cycles. The curve corresponding to the reference cycle shows two successive bumps. The transition between both occurs at about 1350 °C, which is the lowest temperature

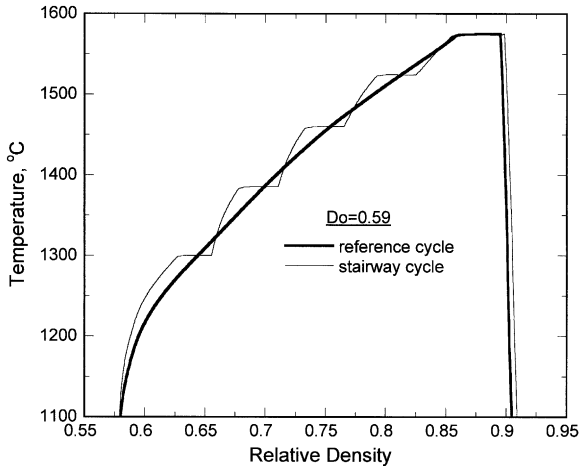

Fig. 4. Comparison of sintering paths during the reference and the stairway cycles.

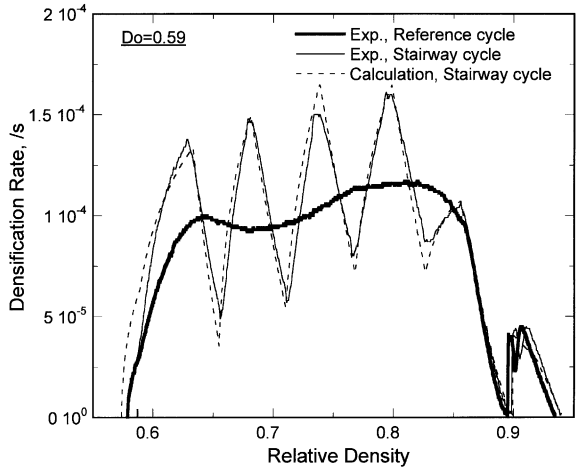

Fig. 5. Densification rate during the reference and the stairway cycles with the reference green density.

of formation of an eutectic in the Al_2O_3–SiO_2–MgO phase diagram.[22] It thus indicates the beginning of liquid phase sintering. At the isothermal sequences the densification rate decreases rapidly. Here, an expression of the densification rate has been obtained by fitting an equation to the isothermal sections of the stairway cycle in Fig. 5. A simple equation has been chosen, which was used by Gillia and Bouvard[15] and is also close to the one used by Hsueh et al.: [23]

$$\dot{\varepsilon}^{s} = \Omega(T)\cdot[D_{\infty}(T) - D]^{n} \tag{9}$$

where $D_{\infty}(T)$ can be considered as the maximum relative density that can be reached during an isothermal test at each temperature. From Fig. 5, it is observed that the densification rate during the isothermal test at each temperature decreases in a set of almost parallel curves. Thus, for simplicity, we fixed the parameter n as the value determined at 1575 °C, i.e. $n = 1.42$. The values of $D_{\infty}(T)$ for each isothermal temperature during the

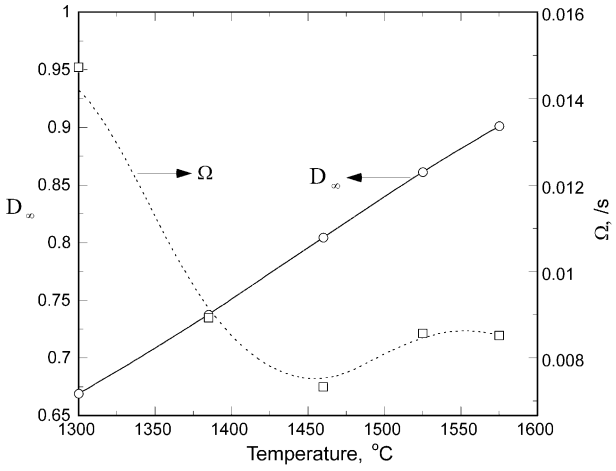

Fig. 6. Evolution of D_{∞} and Ω parameters versus temperature obtained from the stairway cycle with the reference green density.

stairway cycle were determined by finding the values for the best fit of the densification rate data of each isothermal section in Fig. 5. And by using the determined values of $D_{\infty}(T)$, the values of $\Omega(T)$ for each temperature were also determined by finding the values for the best fit of the densification rate data of each isothermal section in Fig. 5.

Fig. 6 shows the evolutions of $D_{\infty}(T)$ and $\Omega(T)$ versus T that have been determined with $n = 1.42$. There may be some arbitrariness in the estimate of $D_{\infty}(T)$, but this arbitrariness does not have much significance as long as the constitutive equation is used in the vicinity of the reference sintering path of relative density versus temperature. The value of $D_{\infty}(T)$ increases monotonically with temperature, however, the evolution of $\Omega(T)$ is not monotonic. $D_{\infty}(T)$ and $\Omega(T)$ can be represented by the following relationships:

$$D_{\infty}(T) = 0.27356\cdot\tanh\left(\frac{T - 1441.48}{303.6}\right) + 0.78793$$

$$\Omega(T) = -8.781116\times10^{-10}\cdot T^{3} + 3.996546\times10^{-6}\cdot T^{2} - 6.052163\times10^{-3}\cdot T + 3.05762$$

where $\Omega(T)$ is the temperature in °C and O is in s^{-1}.

The dashed curve in Fig. 5 shows the calculated results from Eq. (9) making use of the determined representations for values of $D_{\infty}(T)$, $\Omega(T)$ and n. It can be observed that the calculated results represent reasonably well the experimental data for the reference green density sample.

Fig. 7 shows the comparison between experimental data and results calculated by integration of Eq. (9) for the variation of relative density with time for the reference green density sample during the stairway cycle. The constitutive equation gives good representation for the reference green density sample. The error between the

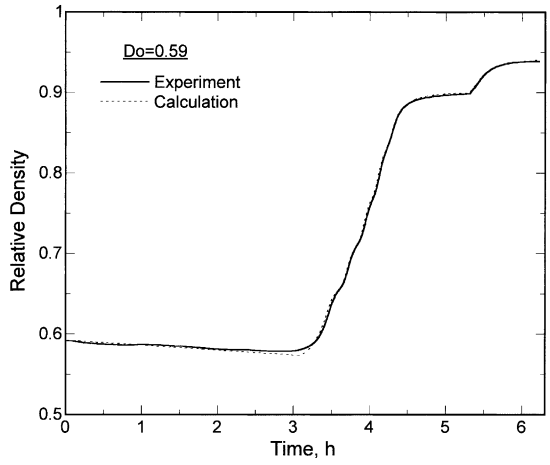

Fig. 7. Comparison of the experimental and theoretical densification curves during the stairway cycle with the reference green density.

experimental data and the calculated result for relative density is smaller than ±1.1%.

However, Eq. (9) has been formulated for a powder compact with reference green density. To investigate the effect of green density, experiments with the stairway cycle have been carried out with compacts of different green densities of 0.53 and 0.67. Fig. 8 shows the densification rate measured during the stairway cycle with green densities of 0.53, 0.59 and 0.67. We found that the density difference regularly decreased during sintering, however, the compacts reach final densities different from each other. We thus assume that the densification rate of a compact can be deduced from the curve obtained for the reference green density through either a contraction or an expansion along the D-axis, depending on whether the green density of this compact is higher or lower than the reference value.[15] This is obtained by introducing the following variable change in Eq. (9):

$$D \rightarrow D_{\mathrm{f,ref}} \cdot \frac{D - D_{\mathrm{o}}}{D_{\mathrm{f}} - D_{\mathrm{o}}} + D_{\mathrm{o,ref}} \cdot \frac{D_{\mathrm{f}} - D}{D_{\mathrm{f}} - D_{\mathrm{o}}} \tag{10}$$

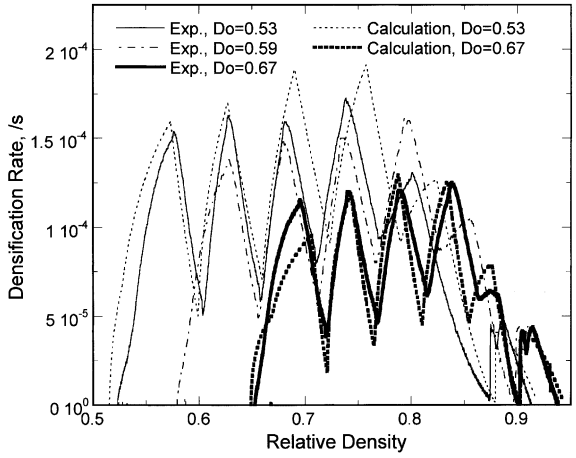

Fig. 8. Comparison of the experimental and theoretical densification rate during the stairway cycle with the different green densities.

where D_{f} is the final density at 1575 °C for each green density. This variable change makes the densification rate curves of lower or higher green densities transform to that of reference green density with the lower limit (green density) and higher limit density (final density at 1575 °C). In Fig. 8, the dotted curves show the calculated results by using the determined parameters [n, $D_{\infty}(T)$, and $\Omega(T)$] for reference green density and the variable change equation, i.e. Eq. (10) for introducing the green density effect. The calculated results represent reasonably well the experimental data for different green density samples. However, it is observed that a relatively large discrepancy happens at 1575 °C due to the largest difference of n values between experimental data and the fixed value of $n = 1.42$ for different green density samples. From experimental data of Fig. 8, it can be observed that the n clearly increases with green density at 1575 °C, however, in the calculation we assumed n as a fixed value for every temperature and green density for simplicity.

Fig. 9 shows the comparison between the experimental data and the calculated results for the variation of relative density with time during the stairway cycle with compacts of different green densities of 0.53 and 0.67. The calculated results (the dotted curves) give reasonably good prediction for the lower and higher green density samples. The errors between experimental data and calculated results for relative density are smaller than ±3.0%.

The variable change equation proposed in this paper, i.e. Eq. (10) has a form alike to that proposed by Gillia and Bouvard[15] for WC–Co mixtures. To consider the effect of green density, Gillia and Bouvard[15] proposed the following variable change equation:

$$D \rightarrow D + \frac{D_{\mathrm{f,rt}} - D}{D_{\mathrm{f,rt}} - D_{\mathrm{o}}} \times \left(D_{\mathrm{o,ref}} - D_{\mathrm{o}}\right) \tag{11}$$

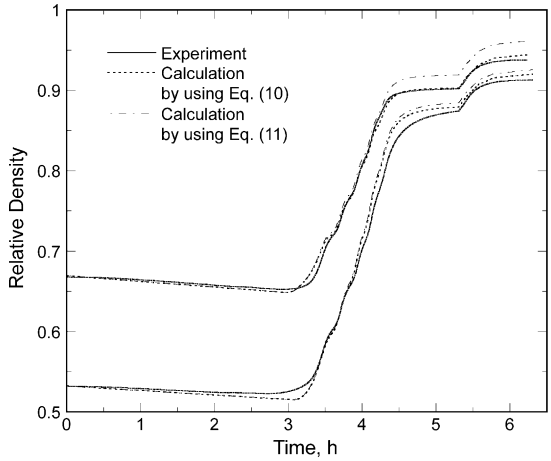

Fig. 9. Comparison of the experimental and theoretical densification curves during stairway cycle with different green densities.

where $D_{f,rt}$ is the final density at room temperature after the experiment. In Fig. 9, the dash-dotted curves are calculated results by using the variable change equation proposed by Gillia and Bouvard,[15] i.e. Eq. (11). The dash-dotted curves do not well predict the experimental data. This discrepancy may be partially due to their having proposed the equation from experimental data of narrow green density variation ($D_o = 0.52$–0.57) and partially due to the different sintering behavior of the materials.

Fig. 10 shows the comparison between the experimental data and the calculated results for the variation of relative density with time during the reference cycle with compacts of different green densities of 0.53, 0.59, and 0.67. The calculated results (the dashed curves) predicted reasonably well the experimental data for three samples. The errors between the experimental data and the calculated results for relative density are smaller than $\pm 3.0\%$ for the low green density sample and $\pm 2.0\%$ for the reference and higher green density samples.

Fig. 11 shows the comparison between the experimental data and the calculated result for the variation of densification rate with relative density during a more complex heating cycle with a reference green density sample. The sample was heated with a rate of 6.2 °C/min up to 1000 °C, 7.5 °C/min up to 1350 °C, 2.6 °C/min up to 1450 °C, and 8.0 °C/min up to 1575 °C. The calculated result (the dotted curve) gives reasonably good prediction. The error between experimental data and calculated result for relative density is smaller than $\pm 1.0\%$.

4.2. Axial viscosity

The axial viscosity, η_z, can be determined from Eq. (5) if the viscoplastic strain rate $\dot{\varepsilon}_z^{vp}$ and the axial stress σ_z are known. Owing to the linearity of the Newtonian

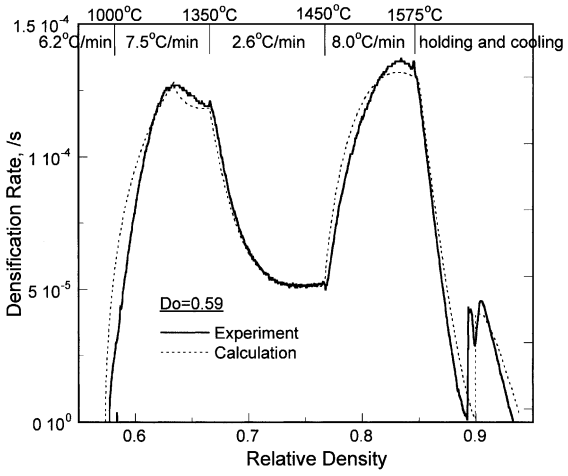

Fig. 11. Comparison of experimental and theoretical densification rates during a more complex heating cycle with the reference green density.

law, $\dot{\varepsilon}_z^{tot}$ is divided into two parts, a sintering contribution $\dot{\varepsilon}_z^{s}$ and the contribution of the load $\dot{\varepsilon}_z^{vp}$, thus the viscoplastic strain rate can be obtained from:

$$\dot{\varepsilon}_z^{vp} = \dot{\varepsilon}_z^{tot} - \dot{\varepsilon}_z^{s} \tag{12}$$

During our experiments, only $\dot{\varepsilon}_z^{tot}$ was measured and, thus, we need to know the contribution of sintering to deduce the viscoplastic strain rate. Fig. 12 shows the variation of the axial strain rate with relative density under intermittent loading at 1400 °C. Here, the following hypothesis was used to determine the axial viscosity. The free axial sintering strain rate can be obtained by connecting the portions of the curve before and after the application of the load. The instantaneous viscoplastic strain rate for a given density is therefore the gap between the free axial strain rate and the recorded rate. Unfortunately, there is clearly a strong transient regime during the entire loading sequence. Thus, the calculation of the viscoplastic strain rate was carried out at

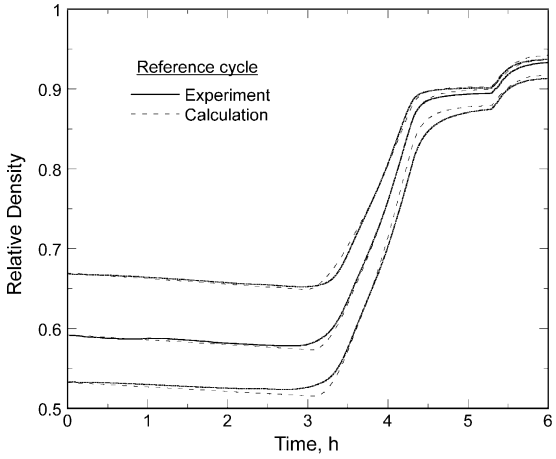

Fig. 10. Comparison of the experimental and theoretical densification curves during the reference cycle with three different green densities.

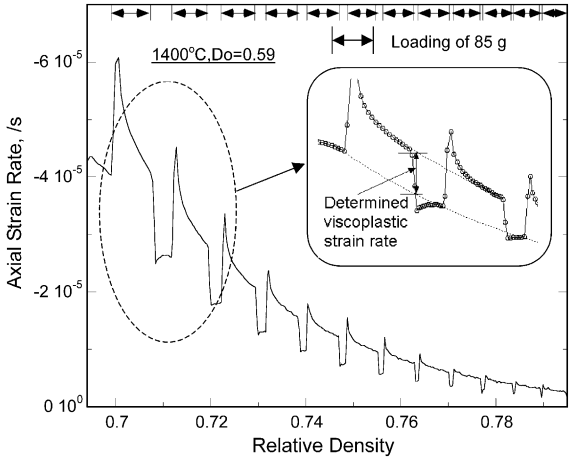

Fig. 12. Axial strain rate recorded during the intermittent loading at 1400 °C with the reference green density.

unloading by using the free axial strain rate fitted with the free axial strain rate data where the effect of loading seems excluded (the later data in unloading sequence), as shown in Fig. 12.

Fig. 13 summarizes the axial viscosity obtained from the experiments of intermittent loading during a long isothermal period at various temperatures. The axial viscosity depends on green density as well as on relative density and temperature. Every isothermal test gives the exponential variation of the axial viscosity with relative density. In Fig. 13, even though it is obvious that the slope decreases as the temperature rises, we assumed the same slope for all temperatures for simplicity. Then, the axial viscosity for reference green density (open data points) may be reasonably well represented by the equation:

$$\eta_z = A_o e^{Q/kT} \cdot e^{B \cdot D} \tag{13}$$

where T is the absolute temperature and k is the Boltzmann's constant. The parameters in Eq. (13) were determined as $A_o = 6.1262 \times 10^{-25}$ MPa·s, Q = 590 KJ/mol, and B = 29.47. To introduce the effect of green density on the axial viscosity, the same variable change equation, i.e. Eq. (10), used in the densification model for free sintering was applied again. The solid, dotted, and dash-dotted curves are the calculated results by using Eqs. (13) and (10) for reference, lower, and higher green density samples, respectively. The calculated results by using Eqs. (13) and (10), represent reasonably well the experimental data for the axial viscosity obtained at various temperatures and with three different green densities.

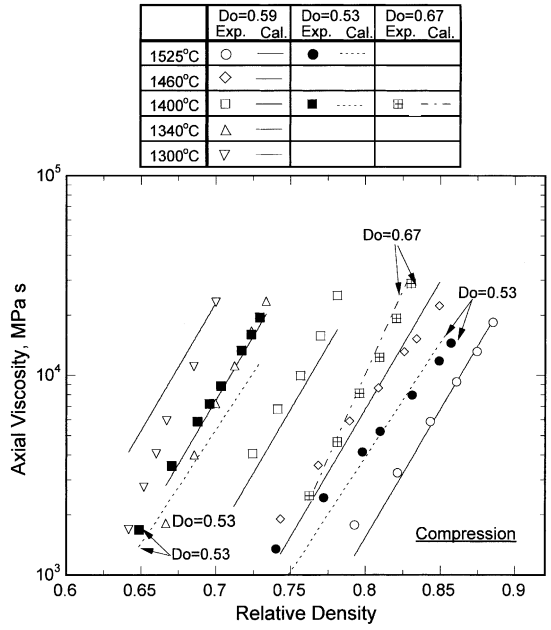

Fig. 13. Comparison of the experimental data and the calculated results for the axial viscosity with different green densities at various temperatures.

4.3. Viscosity obtained from bending test

From elastic theory, the deflection, u, due to the applied load on the center of the three-point bending sample is calculated as follows:

$$u = \frac{1}{4}\left[\frac{F \cdot l^3}{b \cdot h^3}\right]\frac{1}{E} \tag{14}$$

where F, l, b, h, and E are, respectively, the applied force, the distance between the two lower supports of the three-point bending jig, the width and height of the sample, and Young's modulus.

With the elastic–viscous analogy, the deflection increment of a viscous material, Δu, during a time interval, Δt can be estimated by replacing u by $\Delta u/\Delta t$ and E by η in Eq. (14), where η is the viscosity at time t. Thus, the viscosity can be obtained from:

$$\eta = \frac{1}{4}\left[\frac{F \cdot l^3}{b \cdot h^3}\right]\frac{1}{\Delta u/\Delta t} \tag{15}$$

The variation of the deflection, $\Delta u/\Delta t$ in Eq. (15) was obtained from the bending experiment, however, the variations of width and height of the sample could not be measured from the bending experiment. Thus, we also measured the variations of b and h from free sintering of the bending sample. Here, we assumed that the applied load on the bending sample does not affect the densification behavior of the sample.

Fig. 14 summarizes the viscosity obtained from the bending tests of loading during a long isothermal period at various temperatures. For comparison, the axial viscosity obtained from compression tests with reference green density samples is also shown in Fig. 14. Considering the data of 1525 °C, the viscosity increases exponentially with relative density at first, but later it increases rapidly. This may be due to that the deflection of the sample is too large to apply the analogy between

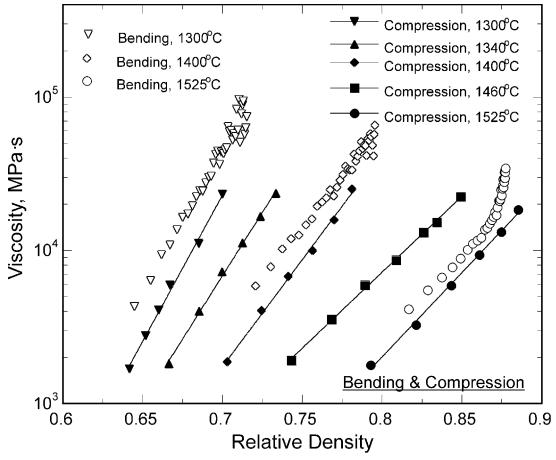

Fig. 14. Viscosity measured from the bending experiments at various temperatures (for comparison, axial viscosities from compression experiment are also shown).

elastic and viscous theories. Thus, it is worth believing the experimental data of the exponential region only at this temperature. It is observed that the viscosity obtained from the bending test shows the same trend (almost the same slope) with that obtained from the compression test, however, the viscosity from the bending test is larger than that from the compression test. The discrepancy may be due to the different stress level. The maximum stress under the bending test is about 0.12 MPa, while that under the compression test is about 0.035 MPa. Similar experimental data, i.e. larger viscosity due to larger applied stress, can be found in the literature by Gillia et al.[16] for WC–Co mixtures under the compression test. Furthermore, in the compression test the applied stress is compressive and almost homogeneous in the sample, while in the bending test the stress is not uniform since it varies from tension to compression along the height. Also, the estimation in the elastic–viscous analogy may be one of the reasons for this discrepancy.

We also obtained the axial viscosity from the compression test and the viscosity from the bending test under loading during the stairway heating cycle. The viscosity was almost consistent with that from the intermittent loading during a long isothermal period. Thus, the data from loading during the stairway heating cycle were not shown in this paper. By experiments with the stairway heating cycle, the viscosity at various temperatures may be obtained easily from faster experiments; however, it is difficult to obtain the variation of viscosity with relative density at the given temperature.

4.4. Viscous Poisson's ratio

Fig. 15 shows variations of axial strain, radial strain, and applied load at 1340 °C for a reference green density sample during compression with repeated displacement loading and pause of displacement. Before the upper punch comes into contact with the sample, the free sintering shrinkage is recorded, i.e. the diameter and height of the sample decrease simultaneously. After the upper punch is set to contact, the force increases and the axial strain decreases at an almost constant strain rate and the radial strain increases rapidly during the period of displacement loading. However, during the period of pause of displacement, the force decreases rapidly, the axial strain stays as a constant value, and the radial strain decreases due to sintering shrinkage. The effect of free sintering on the radial strain during the period of pause progressively disappears with time.

According to the partition of the strain rate, viscous Poisson's ratio is rewritten as:

$$\nu^{\mathrm{vp}} = -\frac{\dot{\varepsilon}_{\mathrm{r}}^{\mathrm{total}} - \dot{\varepsilon}_{\mathrm{r}}^{\mathrm{s}}}{\dot{\varepsilon}_{z}^{\mathrm{total}} - \dot{\varepsilon}_{z}^{\mathrm{s}}} \tag{16}$$

During experiment, $\dot{\varepsilon}_{\mathrm{r}}^{\mathrm{total}}$ and $\dot{\varepsilon}_{z}^{\mathrm{total}}$ are measured continuously. To estimate the free sintering radial strain rate, $\dot{\varepsilon}_{\mathrm{r}}^{\mathrm{s}}$ during the loading periods, the radial shrinkage rates before and after a loading period were used. However, the free sintering axial strain rate was assumed to be zero during the periods of displacement loading since the axial strain rate due to displacement loading is much higher than the free sintering axial strain rate that may exist during the loading periods.

Fig. 16 shows the variation of the viscous Poisson's ratio with relative density at 1340 °C for reference, lower, and higher green density samples. The viscous Poisson's ratio increases with relative density, but converges to 0.5 as relative density reaches a certain relative density, $D_{\infty}^{'}$, that depends on green density. Bordia and Scheror[24] extensively overviewed the variation of the viscous Poisson's ratio with relative density by using various densification models. According to them, the viscous Poisson's ratio converges to 0.5 as relative density goes to

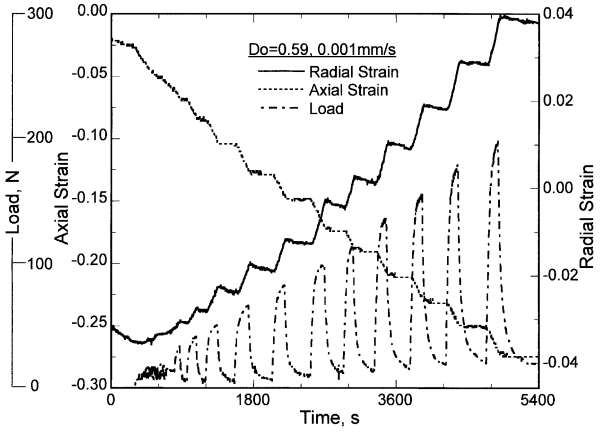

Fig. 15. The variations of axial strain, radial strain, and load with time during the compression test at 1340 °C.

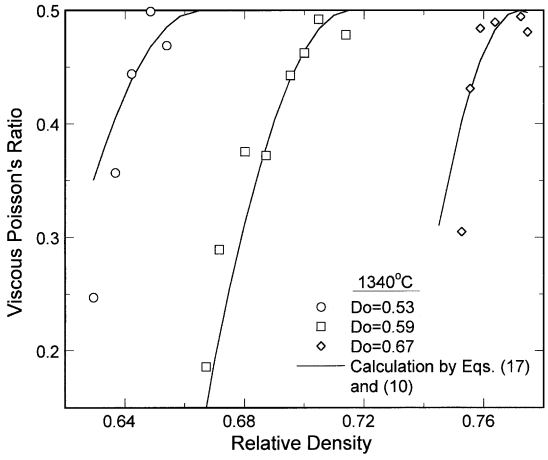

Fig. 16. Comparison of the experimental data and the calculated results for the viscous Poisson's ratio with three different green densities at 1340 °C.

1 since they considered that the powder compact underwent full densification. In our case, the powder compact is able to densify until a certain maximum relative density (much lower that 1) that may depend on temperature, green density, and the applied stress. This maximum relative density has been called D_∞ for free sintering in Section 4.1 in this paper. In this experiment, since the applied axial stress goes up to 6.4 MPa during the displacement loading periods, the maximum relative densities at 1340 °C increased a little when compared with those under free sintering for each green density sample. The average increment in the maximum relative densities of reference, lower, and higher green density samples was about 0.0134; thus, we assumed $D'_\infty = D_\infty + 0.0134$ for each green density samples. The viscous Poisson's ratio with reference green density may be represented by the following equation:

$$\nu^{vp} = 0.5 - A_v \cdot \left(D - D'_\infty\right)^{n_v} \text{ at } 0.67 < D < 0.717 \quad (17)$$

where, A_v and n_v are, respectively, determined as 150 and 2. To introduce the effect of green density on the viscous Poisson's ratio, the same variable change equation, i.e. Eq. (10) used in the densification model for free sintering was also applied on relative density, D and the maximum density, D'_∞. The solid lines are the calculated results by using Eqs. (17) and (10) for three different green density samples. The calculated results by using Eqs. (17) and (10) represent reasonably well the experimental data for the viscous Poisson's ratio obtained from three different green densities at 1340 °C. When the experimental temperature changes, A_v and n_v as well as the increment in the maximum relative density may change. Thus, for more general equation for viscous Poisson's ratio, more experiments at higher temperatures seem to be needed.

5. Conclusion and perspectives

Sintering tests have been performed on alumina powder compacts with three different green densities to investigate the densification kinetics of a powder system. From the results of these tests, a simple equation has been formulated, which expresses the densification rate under free sintering as a function of temperature, relative density and green density. It contains two parameters as functions of temperature and one temperature independent parameter. The densification behavior predicted by this constitutive equation has been compared with experimental data for compacts of green densities between 0.53 and 0.67. The agreement is particularly satisfactory.

The viscosity of alumina powder compacts during sintering was investigated by using the intermittent loading method under a compression test and a bending test. Every isothermal test gives an exponential variation of viscosity with relative density. A general equation was proposed for the axial viscosity of an alumina compact as a function of temperature, relative density, and green density.

The viscous Poisson's ratio of alumina powder compacts during sintering was investigated under compression at 1340 °C by using CCD video camera. The viscous Poisson's ratio increases with relative density, but converges to 0.5 as the compact reaches a certain maximum relative density that may depend on temperature, green density, and the applied stress. A parabolic equation was proposed for the viscous Poisson's ratio of alumina compacts with three different green densities at 1340 °C.

This set of data for the free sintering densification rate, the axial viscosity and the viscous Poisson's ratio makes it possible to identify the parameters of a constitutive equation with a Newtonian form. Note that the same type of equations has already been used for describing the sintering of different powder materials, in particular tungsten carbide/cobalt mixtures. The constitutive equation proposed in this paper has been implemented in a finite element code. With this code it has thus been possible to investigate the shape change of a complex shaped alumina powder compact due to heterogeneous green density field.[25]

Acknowledgements

The authors thank Claude Carry, Georges Kapelski and Guillaume Bernard-Granger for helpful discussions and support.

References

1. Schwartz, M. M., *Handbook of Structural Ceramics*. McGraw-Hill, New York, 1992.
2. Coble, R. L., Diffusion models for hot pressing with surface energy and pressure effects as driving forces. *J. Appl. Phys*, 1970, **41**, 4798–4807.
3. McHugh, P. E. and Riedel, H., A liquid phase sintering model: application to Si_3N_4 and WC–Co. *Acta Mater*., 1997, **45**, 2995–3003.
4. Su, H. and Johnson, D. L., Master sintering curve: a practical approach to sintering. *J. Am. Ceram. Soc*., 1996, **79**, 3211–3217.
5. Helle, A. S., Easterling, K. E. and Ashby, M. F., Hot-isostatic pressing diagrams: new developments. *Acta metall*, 1985, **33**, 2163–2174.
6. Kwon, Y. S. and Kim, K. T., High-temperature densification forming of alumina powder-constitutive model and experiments. *ASME J. Eng. Mat. Tech*., 1996, **118**, 448–455.
7. Olevsky, E. A., German, R. M. and Upadhyaya, A., Effect of gravity on dimensional change during sintering—II. Shape distortion. *Acta Mater*., 2000, **48**, 1167–1180.
8. Liu, J., Liu, Y., Lal, A. and German, R. M., Shape distortion induced by gravity in the initial stage of solid phase sintering. *Scripta Materialia*, 1999, **40**, 1221–1227.

9. Kim, H. G., Lee, H. M. and Kim, K. T., Near-net-shape forming of ceramic powder under cold combination pressing and pressureless sintering. *ASME J. Eng. Mat. Tech.*, 2001, **123**, 221–228.
10. Cannon, R. M. and Carter, W. C., Interplay of sintering microstructures, driving forces, and mass transport mechanisms. *J. Am. Ceram. Soc.*, 1989, **72**, 1550–1555.
11. Exner, H. E. and Bross, P., Material transport rate and stress distribution during grain boundary diffusion driven by surface tension. *Acta Metall*, 1979, **27**, 1007–1012.
12. Bouvard, D. and McMeeking, R. M., Deformation of Interparticle Necks by Diffusion-Controlled Creep. *J. Am. Ceram. Soc.*, 1994, **79**, 666–672.
13. Svoboda, J., Riedel, H. and Zipse, H., Equilibrium pore surfaces, sintering stresses and constitutive equations for the intermediate and late stages of sintering. I. Computation of equilibrium surfaces. *Acta Metall. Mater.*, 1994, **42**, 435–443.
14. Exner, E. and Kraft, T., Proceedings of the Powder Metallurgy World Congress. *Granada EPMA*, 278–283.
15. Gillia, O. and Bouvard, D., Phenomenological analysis of densification kinetics during sintering: application to WC–Co mixture. *Mat. Sci. Eng. A*, 2000, **A279**, 185–191.
16. Gillia, O., Josserond, C. and Bouvard, D., Viscosity of WC–Co compacts during sintering. *Acta Mater.*, 2001, **49**, 1413–1420.
17. Du, Z. Z. and Cocks, A. C. F., Constitutive models for the sintering of ceramic components. II. Sintering of inhomogeneous bodies. *Acta Metall. Mater.*, 1992, **40**, 1981–1994.
18. Riedel, H., Sun, D.-Z., Numerical Methods in Industrial Forming Processes. In: J. L., Chenot, D., Wood, O. C., Zienkiewicz. Eds. Balkema, Rotterdam1992, 883
19. Olevsky, E. A., Theory of sintering: from discrete to continuum. *Mater. Sci. Eng. Report*, 1998, **23**, 41–99.
20. Richerson, D. W., *Modern Ceramic Engineering : Properties, Processing and Use in Design*. M. Dekker, New York, 1982.
21. Cai, P. Z., Messing, G. L. and Green, D. J., Determination of the mechanical response of sintering compacts by cyclic loading dilatometry. *J. Am. Ceram. Soc.*, 1997, **80**, 445–452.
22. Kingery, W. D., Bowen, H. K. and Uhlmann, D. R., *Introduction to Ceramics*. John Willey & Sons, Singapore, 1975.
23. Hsueh, C. H., Evans, A. G., Cannon, R. M. and Brook, R. J., Viscoelastic stresses and sintering damage in heterogeneous powder compacts. *Acta. Metall*, 1986, **34**, 927–936.
24. Bordia, R. K. and Scheror, G. W., On constrained sintering—II. Comparison of constitutive models. *Acta. Metall*, 1988, **36**, 2399–2409.
25. Kim, H. G., Gillia, O. G., Doremus, P. and Bouvard, D., Finite element analysis for compaction and sintering of an alumina powder compact. *Int. J. Mech. Sci.*, accepted for publication.